

Maximizing Performance of Quantum Cascade Laser-Pumped Molecular Lasers


Fan Wang,¹ Steven G. Johnson^{1,2} and Henry O. Everitt^{3,4,*}

¹*Department of Mathematics, Massachusetts Institute of Technology, Cambridge, Massachusetts 02139, USA*

²*Department of Physics, Massachusetts Institute of Technology, Cambridge, Massachusetts 02139, USA*

³*Department of Physics, Duke University, Durham, North Carolina 27708, USA*

⁴*U.S. Army CCDC Aviation and Missile Center, Redstone Arsenal, Alabama 35898, USA*

 (Received 26 January 2021; revised 8 June 2021; accepted 6 July 2021; published 6 August 2021; corrected 27 January 2022)

Quantum-cascade-laser- (QCL) pumped molecular lasers (QPMLs) have recently been introduced as a source of powerful (> 1 mW) tunable (> 1 THz) narrow-band (< 10 kHz) continuous-wave terahertz radiation. The performance of these lasers depends critically on molecular collision physics, pump saturation, and on the design of the laser cavity. Using a validated three-level model that captures the essential collision and saturation behaviors of the QPML gas nitrous oxide (N_2O), we explore how the threshold pump power and output terahertz power depend on the pump power and gas pressure, as well as on the diameter, length, and output-coupler transmissivity of a cylindrical cavity. The analysis indicates that maximum power occurs as pump saturation is minimized in a manner that depends much more sensitively on pressure than on cell diameter, length, or transmissivity. A near-optimal compact laser cavity can produce tens of milliwatts of power tunable over frequencies above 1 THz when pumped by a multiwatt QCL.

DOI: [10.1103/PhysRevApplied.16.024010](https://doi.org/10.1103/PhysRevApplied.16.024010)

I. INTRODUCTION

The need for powerful tunable narrow-band sources to span the “terahertz gap” between 0.3 and 3.0 THz continues to grow as next-generation wireless-communication systems demand increasing bandwidth and new opportunities arise for intrinsically short-range communications facilitated by strong frequency-dependent atmospheric-water-vapor absorption [1]. Most terahertz sources fall into one of two categories: lower-frequency electronic sources for which power decreases with increasing frequency, such as microwave oscillators or frequency multipliers [2], backward-wave oscillators [3], and gyrotrons [4] and higher-frequency optical sources for which power increases with increasing frequency, such as terahertz quantum cascade lasers [5] and difference-frequency lasers [6–8]. The region in between, where powerful sources are lacking, is known as the terahertz gap.

Recently, one of the original sources of terahertz radiation, gas-phase optically pumped far-infrared lasers (OPFIRs), has experienced a revival as the line-tunable CO_2 pump laser has been replaced by a continuously tunable quantum cascade laser (QCL) [9–12]. By this substitution, virtually any rotational transition of a gas-phase molecular gain medium may be made to lase if pumped

by a QCL tuned into coincidence with the associated infrared molecular rotation–vibration transition. Unlike electronic sources, the Manley-Rowe effect in these QCL-pumped molecular lasers (QPMLs) causes the power to increase with increasing frequency. Consequently, reports of power exceeding 1 mW [13] and tunability approaching 1 THz [12] from QPMLs foreshadow the potential of these sources to span the terahertz gap.

In order to ascertain the potential of these sources, we must explore how the output power may be maximized. It is well known that the threshold pump power and terahertz output power depend sensitively on the pressure of the molecular gain medium [12,14–19]. What is not as well known is how output power depends on cavity geometry (diameter, length, output-coupler transmissivity) and how those parameters determine the optimal pressure for obtaining maximal power. Recently, a comprehensive physics-based experimentally validated model has been developed [19] that fully captures the interplay of thousands of thermally populated rotational states connected by millions of collisional energy transfer channels in the laser. However, the complexity of that model limits its utility for building the intuition and analytical insights necessary to understand the sensitivity of output power on these factors. Alternatively, in Ref. [12], a simple three-level model has been proposed to describe the essential lasing behavior for the compact QPMLs in the limiting case of very low pressures, for which the dominant relaxation mechanism is molecule-wall collisions and $\alpha_{\text{IR}}L \ll 1$, where α_{IR} is

*heveritt@duke.edu

the IR pump absorption coefficient and L is the cavity length.

To capture the behavior of QPMLs at higher pressures where maximal terahertz power may be obtained, a more rigorous version of this three-level model, which includes dipole-dipole collisions, molecule-wall collisions, and pump saturation, is presented here. This improved treatment, validated against the comprehensive model, allows us to study the laser performance across the entire pressure regime and to provide deep insights for optimizing cavity design. After using this improved model to identify the optimal cavity geometry, we show that a much smaller, cigar-sized cavity can achieve 95% of the optimal performance, a necessary step toward the technological viability of the QPML concept. We then demonstrate the potential for QPMLs to produce tens of milliwatts of continuous-wave narrow-band power tunable over frequencies above 1 THz using multi-watt QCLs that are, or soon will become, commercially available.

Figure 1(a) schematically illustrates the QPML system. After passing through the front mirror, the QCL pump beam excites the molecular gain medium within the copper-tube laser cavity of radius R_{cell} and length L . The rotational lasing transition of the gain molecule is brought into resonance with the cavity by a back mirror that adjusts the cavity length. The terahertz laser power emerges from the same front mirror with transmission coefficient T_{THz} (hereafter referred to as T unless specified otherwise), after which it is detected by a Schottky-diode detector or heterodyne receiver. We envision the output coupler as a copper reflector with a centered pinhole through which both beams pass; however, the analysis presented here does not require this geometry, only that the infrared and terahertz input-output transmissivities of the cavity are known.

Throughout the paper, N_2O is adopted as the gain molecule because of the simplicity of its rotational energy-level structure, large infrared absorption coefficients, and experimentally demonstrated performance as a broadly tunable QPML [12]. However, the revised three-level model presented below, and the design principles derived from it, are universal and may be easily applied to other candidate linear molecules such as HCN, OCS, and CO. Extension of this model to more complex QPML molecules such as NH_3 and CH_3F may also be made, requiring the inclusion of additional collisional relaxation processes and rates, but the results derived herein may be applied to those molecules without loss of generality. As has been discussed previously [12], the tuning range, pump threshold power, and output power depend on the rotational energy-level spacings of the molecule, its infrared absorption coefficients, its dipole moment, and the gas pressure p . What has not been explored, and is discussed extensively below, is how this also depends on the pump

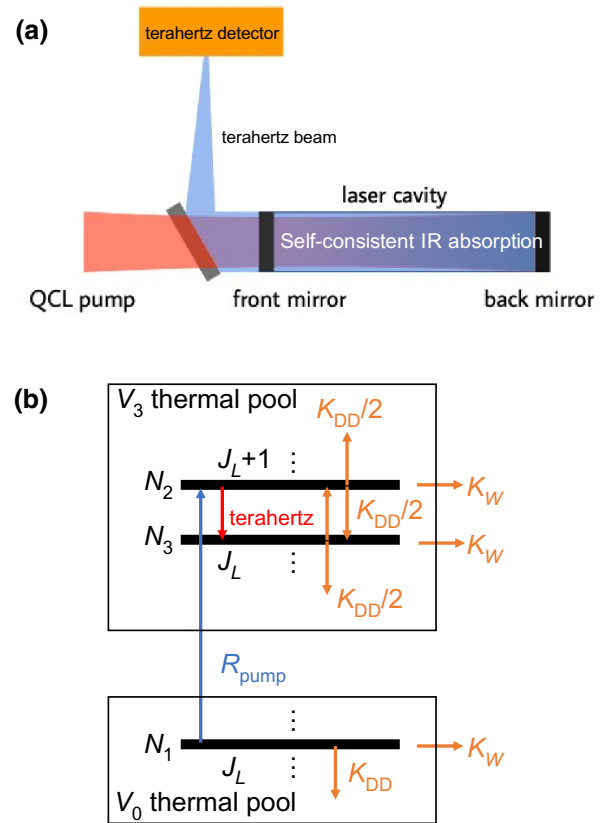


FIG. 1. (a) The schematics of the QCL-pumped molecular laser. The QCL pumps a cylindrical metallic laser cavity with radius R_{cell} and length L , filled with molecular gas with pressure p . If the pump power exceeds the threshold, terahertz radiation is generated and emitted through a front mirror with transmission coefficient T . (b) A three-level model that describes the essential physics of the QPML system. Molecules in rotational level 1 from the ground vibrational state v_0 are pumped into rotational level 2 of the excited vibrational state v_3 by the infrared QCL laser, generating terahertz emission between levels 2 and 3 until quenched by dipole-dipole (rate k_{DD}) and molecule-wall collisions (rate k_w).

power, pump saturation, cavity geometry R_{cell} and L , and output-coupler transmissivity T .

In the following sections, we first provide an overview of the key physical processes that must be captured in the model. Then, we describe in detail the rate equation for obtaining the population inversion, pump saturation, and gain coefficient, and the approach for computing the pump threshold power, output power, and laser efficiency. We show that the results obtained from the three-level model agree well with the comprehensive model, with a peak-power difference less than 15%. Then, a full discussion on the cavity design is presented, focusing on the cavity loss, cavity dimensions, and output-coupler transmission over different laser transitions.

II. LASER-MODEL OVERVIEW

A theoretical model describing the behavior of a QPML must account for the molecular collisional relaxation mechanisms that operate among the many thermally populated rotational states and act to quench the QCL-pumped inversion. There are dozens of such thermally populated rotational states in the ground vibrational manifold of N_2O and dozens more in the excited vibrational level when pumped by the QCL. This suggests that hundreds of collisional thermalization channels exist among those levels and are faithfully represented in the previously developed comprehensive model that describes how the QPML power and threshold depend on pump power, pressure, and cavity parameters [19]. However, in the very-low-pressure regime where molecular collisions with the wall of the laser cavity are more frequent than intermolecular collisions, only the rotational states directly connected by the QCL pump or QPML transition experience significant pump-induced population changes. Consequently, it has been shown that a simple three-level model captures the salient QPML dependence on molecular and cavity parameters in this very-low-pressure regime [12]. The improved three-level model introduced here extends its applicability to higher pressures by explicitly including the effects of intermolecular collisions and pump saturation. Its viability as a descriptive model is ascertained by comparing its predictions to those of the comprehensive model.

Figure 1(b) depicts the three-level model proposed in this work. The population of these levels is partitioned into thermal and nonthermal contributions, respectively representing the unpumped and pumped molecules. Simply stated, the rotational populations of which can or cannot be represented by a Boltzmann distribution. N_1 , N_2 , and N_3 are the nonthermal populations induced by the pump for the three rotational levels. The total population for level i is the summation over thermal and nonthermal populations $N_i^{\text{tot}} = N_i + N_i^{(0)}$, where $N_i^{(0)}$ is the thermal population without the pump. The QCL excites a rovibrational transition from rotational level 1 with quantum number J_L in the ground vibrational state to rotational level 2 in the excited vibrational state v_3 in N_2O . The rotational quantum number of level 2 is determined by the type of rovibrational transition excited by the QCL: for P -, Q -, and R -branch transitions, $J_2 = J_L - 1$, J_L , and $J_L + 1$, respectively. Without loss of generality, we only consider the R -branch excitation here, so the rotational quantum numbers of levels 2 and 3 are $J_L + 1$ and J_L , respectively. By using a continuously tunable midinfrared QCL, every thermally populated ground-state rotational level J_L may be pumped, inducing the corresponding v_3 rotational transitions $J_L + 1 \rightarrow J_L$ to lase, making broad terahertz tunability a reality [12]. (This paper does not address lasing arising from the ground-state refilling transitions $J_L + 1 \rightarrow J_L$.) The laser frequency is

$\nu_{\text{THz}} \approx 2B(J_L + 1)$, where B is the rotational constant. For N_2O , $2B \approx 24.9$ GHz.

The dominant collisional-relaxation processes for the pressure range considered here (< 1 Torr) are the dipole-dipole and molecule-wall collisions. For linear molecules, the branching ratio for rotational transitions following dipole-dipole collisions is $\rho_{J \rightarrow J+1} = (J + 1)/(2J + 1)$ and $\rho_{J \rightarrow J-1} = J/(2J + 1)$. For $J > 10$, we can approximate $\rho_{J \rightarrow J+1} \approx \rho_{J \rightarrow J-1} \approx 1/2$ and hence the dipole-dipole collision rate is $k_{\text{DD}}/2$, as shown in Fig. 1. Here, $k_{\text{DD}} = \sigma_{\text{DD}} n_{\text{tot}} \langle v \rangle$, where $\sigma_{\text{DD}} = 35 \text{ \AA}^2$ is the dipole-dipole collision cross section for N_2O , n_{tot} is the total population density (proportional to the molecular pressure), and $\langle v \rangle$ is the thermally averaged relative velocity between molecules. The other half of the dipole-dipole collisions (up from level 2 and down from level 3) transfer population into the v_3 vibrational “thermal pool” [15,16,19], a collection of rotational levels the total population of which may rise and fall in response to the action of the pump but the relative rotational population distribution of which remains in thermal equilibrium with a Boltzmann distribution. As noted above, the thermal pool adds thermally distributed population into levels 2 and 3 that tends to quench the QCL-induced nonthermal population inversion. However, as is discussed below, the nonthermal population in N_2O dominates and the thermal population is negligible.

Molecule-wall collisions are also an important pathway for relaxation, especially in a compact laser cavity. In the low-pressure limit, the molecular mean free path λ_M is larger than the cylindrical-cavity radius R_{cell} , so pressure-independent ballistic collisions with the wall are dominant. At higher pressures where $\lambda_M < R_{\text{cell}}$, molecules diffuse to the walls at a rate that decreases inversely with pressure. The wall-collision rate used here is the minimum of the ballistic ($k_w = 2\langle v \rangle_{\text{abs}}/3R_{\text{cell}}$) and diffusive ($k_w = 2\langle v \rangle_{\text{abs}}\lambda_M/3R_{\text{cell}}^2$) wall rates, where $\langle v \rangle_{\text{abs}}$ is the average absolute velocity of the molecule and the factor of $2/3$ is a geometrical factor accounting for the radial velocities in the cylindrical cavity [20].

For N_2O , numerous vibrational levels lie below and above the excited v_3 level pumped by the QCL. Vibrational-state changing (or “v-v”) collisions among the thermal pools of these levels are another significant relaxation process, especially at higher pressures, when their rate, which grows linearly with pressure, exceeds the rate of wall collisions. These v-v collisions represent a potential advantage of N_2O over molecules such as CH_3F and NH_3 , which have no intermediate vibrational levels between the ground and pumped vibrational levels. Consequently, as pressure increases and the diffusive wall collision rate slows, pumped population accumulates in the thermal pool and quenches the inversion [15,19]. Although this “vibrational bottleneck” is negligible over the range of low pressures in which the N_2O laser operates, these additional

v-v relaxation pathways need to be included in the model at very high pressures or for other molecules such as CH₃F and NH₃.

Note that spontaneous emission from rotational levels is neglected when computing the population inversion in our three-level model. In these long-wavelength collision-dominated molecular-gas lasers, the spontaneous-emission rate ($1/t_{sp} \sim 10^{-5} \text{ s}^{-1}$) is negligible compared with the dipole-dipole collision rate ($k_{DD} \sim 10^5 \text{ s}^{-1}$). Therefore, the spontaneous-emission rate between levels 2 and 3 is used only for the gain calculation.

Of paramount importance for understanding lasing in compact cavities is the effect of pump saturation on the QCL-pumped infrared rovibrational transition. As the pump moves significant population from level 1 to level 2, the infrared-absorption coefficient α_{IR} decreases as $N_1 - N_2$ decreases. Since the QCL pump decays along the cavity axis exponentially as $\exp(-\alpha_{IR}L)$, a decreasing α_{IR} means an increasingly transparent gas and a greater penetration depth for the QCL pump. This pump-saturation effect, which is greatest for low-pressure operation in short small-diameter cavities, depends on the pump rate, which also depends on α_{IR} . Consequently, the nonlinear effects of pump saturation must be ascertained self-consistently using an iterative nonlinear-equation algorithm.

III. THREE-LEVEL MODEL EQUATIONS

The rate equations for N_i as shown in Fig. 1(b) are

$$\begin{aligned} \frac{dN_1}{dt} &= -R_{\text{pump}} - N_1(k_{DD} + k_w), \\ \frac{dN_2}{dt} &= R_{\text{pump}} - N_2(k_{DD} + k_w) + N_3k_{DD}/2, \\ \frac{dN_3}{dt} &= N_2k_{DD}/2 - N_3(k_{DD} + k_w). \end{aligned} \quad (1)$$

At steady state, $dN_1/dt = dN_2/dt = dN_3/dt = 0$, so that

$$\begin{aligned} N_1 &= -\frac{R_{\text{pump}}}{k_{DD} + k_w}, \\ N_2 &= R_{\text{pump}} \frac{k_{DD} + k_w}{(3k_{DD}/2 + k_w)(k_{DD}/2 + k_w)}, \\ N_3 &= R_{\text{pump}} \frac{k_{DD}/2}{(3k_{DD}/2 + k_w)(k_{DD}/2 + k_w)}, \end{aligned} \quad (2)$$

and the population inversion between levels 2 and 3 is

$$\Delta N = N_2 - N_3 = \frac{R_{\text{pump}}}{3k_{DD}/2 + k_w}. \quad (3)$$

Here, the pump rate for QCL power P_{QCL} is

$$R_{\text{pump}} = \frac{\beta P_{\text{QCL}}}{h\nu_{\text{IR}}} \frac{1}{\pi R_{\text{cell}}^2 L}, \quad (4)$$

in which β is the fraction of pump power absorbed in the cavity. β depends on P_{QCL} , pressure, α_{IR} , and L in a complex manner. In the low-pressure limit, with consideration of only a single pass in the cavity as in Ref. [12], $\beta \approx \alpha_{\text{IR}}L \ll 1$. More generally, the QCL beam reflects from the back and front mirrors and, over multiple bounces, can travel much farther than L . As pressure increases, so does α_{IR} , effectively reducing the number of bounces by the QCL beam. For increasing pressure, α_{IR} , or L , β approaches 1, so the entire pump beam is absorbed. To capture these effects, including pump saturation and round-trip bounces and losses, a more accurate description of the pump absorption is provided next.

With a given α_{IR} , β can be obtained by summing contributions over all round trips as

$$\beta = (1 - e^{-\alpha_{\text{IR}}L}) \frac{(1 + R_1 e^{-\alpha_{\text{IR}}L})}{1 - R_1 R_2 e^{-2\alpha_{\text{IR}}L}}, \quad (5)$$

where R_1 and R_2 are the IR reflection coefficients from the back and front mirrors, respectively. Note that β , which is simply the Beer's law absorption multiplied by a term that accounts for multiple round trips, includes both molecular (α_{IR} , pressure) and cavity (R_1 , R_2 , L) contributions. Thus, the fractional pump power absorbed depends on and may be adjusted by any of these parameters. For a copper mirror, we approximate $R_1 = 0.95$ and $R_2 = T_{\text{IR}}R_1$, with $T_{\text{IR}} = 0.96$ (4% leaking out of the front mirror). Since β in Eq. (5) determines the pump rate [Eq. (4)] and the populations N_1 and N_2 [Eq. (2)], it affects the IR pump absorption coefficient α_{IR} nonlinearly. α_{IR} at the pump frequency ν_{IR} is evaluated by

$$\alpha_{\text{IR}} = \frac{8\pi^3 \nu_{\text{IR}}}{3hc} |(1|\mu|2)|^2 (N_1^{\text{tot}} - N_2^{\text{tot}}) S(\nu_{\text{IR}}, \nu_0), \quad (6)$$

in which $N_1^{\text{tot}} = N_1^{(0)} + N_1$ and $N_2^{\text{tot}} = N_2^{(0)} + N_2$ are the total (thermal + nonthermal) populations of levels 1 and 2, $|(1|\mu|2)|^2$ is the dipole matrix element for the pump transition obtained from the HITRAN database [21], and $S(\nu_{\text{IR}}, \nu_0)$ is the absorption line-shape function, obtained by convolving the spectral hole burning (SHB) and the Gaussian Doppler line-shape functions. For IR absorption, the SHB line shape is a Lorentzian obtained by convolution of two other Lorentzians: the pressure-broadening line shape with half width $\Delta\nu_p$ and the QCL line width with half width $\Delta\nu_{\text{QCL}}$, summed together as $\Delta\nu_{\text{SHB}} = \Delta\nu_p + \Delta\nu_{\text{QCL}}$. $S(\nu_{\text{IR}}, \nu_0)$, which is usually described by a Voigt profile, is empirically approximated here by a Lorentzian with width $\Delta\nu_S = \sqrt{\Delta\nu_D^2 + \Delta\nu_{\text{SHB}}^2}$. This approximation underestimates the effect of pump saturation at very low pressures, but as $\beta \rightarrow 1$, all pump photons are absorbed irrespective of the line-shape approximation used. For N₂O, $\Delta\nu_p = 4 \text{ MHz/Torr}$, and $\Delta\nu_D = 3.58 \times$

$10^{-7} \nu_0 \sqrt{T_e/M}$, in which ν_0 is the IR transition frequency (both megahertz), $T_e = 300$ K is the temperature, and $M = 44$ amu is the molecular mass. The line width of the pump QCL is assumed as $\Delta\nu_{\text{QCL}} = 1$ MHz [12].

The saturation-dependent infrared absorption coefficient for a given transition is obtained by nonlinearly solving Eqs. (3)–(6). The pump saturation is described in Eq. (6) by the population difference ($N_1^{\text{tot}} - N_2^{\text{tot}}$) between levels 1 and 2. As mentioned above, level 1 depletes and level 2 fills as the pump power increases, so that ($N_1^{\text{tot}} - N_2^{\text{tot}}$) and α_{IR} decrease. Figure 2 plots typical fractional IR absorption curves as a function of the pump power for three N_2O pressures. As expected, α_{IR} decreases as the pump power increases, allowing more round trips of the IR beam inside the cavity. This pump saturation is more significant at lower pressures because there is less population in level 1 and the SHB is narrower. It can be seen that the saturation increases almost quadratically with decreasing pressure. Note that some infrared power is lost on each round trip through absorption by the cavity walls and through the output coupler, so less of the infrared beam is absorbed by the gas in multiple round trips than in a cavity long enough for single-pass absorption. Indeed, in the limit of an empty cavity, the IR beam may only execute $(1 + R_1)/(1 - R_1R_2)$ round trips (14.6 for the values of R_1 and R_2 presented above) before being fully lost by the cell itself. The inset illustrates these behaviors by plotting the relation between the fractional loss $[-\ln(1 - \beta)]$ and the cavity length L for a typical pumped transition. Without pump saturation and round trips in the cavity, one expects from Eq. (5) a linear curve $-\ln(1 - \beta) \approx$

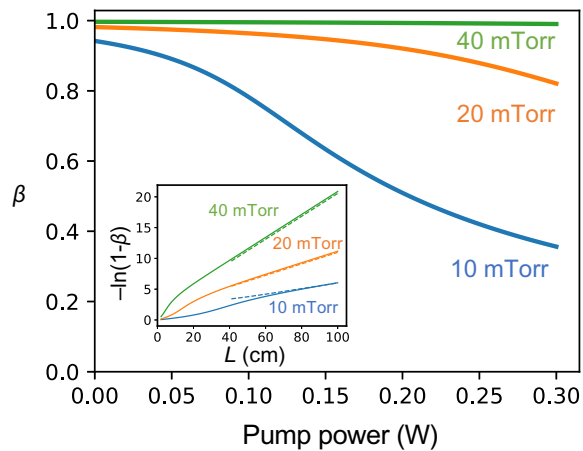


FIG. 2. The fractional IR absorption β varies with pump power, for three different molecular pressures. In the calculation, $J_L = 14$ is pumped with cavity geometry $R_{\text{cell}} = 0.25$ cm and $L = 15$ cm. The inset shows how the IR absorption changes with the cavity length L for different molecular pressures. The dashed lines plot $[\alpha_{\text{IR}}L - \ln(1 - R_1)]$ for the three pressures, showing an asymptotic linear relation between $[-\ln(1 - \beta)]$ and L for longer cavities.

$\alpha_{\text{IR}}L + \ln(1 - R_1)$, the slope of which is the IR absorption coefficient, which increases linearly with pressure and L for $L > 30$ cm. The dashed lines in the inset of Fig. 2 plot $[\alpha_{\text{IR}}L - \ln(1 - R_1)]$ for the three pressures, confirming this asymptotic linear relation. For shorter cavities, pump saturation and multiple round trips produce larger cavity losses and reduce the fraction of pump power β absorbed by the molecular gain medium.

Note that in the three-level model, molecules transfer from levels 2 and 3 into the thermal pool with rate $k_{\text{DD}}/2$, as shown in Fig. 1. For N_2O , the thermal pool relaxes to the ground state with rate $k_{\text{pool}} = k_w + k_{\text{v-v}}$ through wall and v-v collisions. To obtain the v-v transition rate $k_{\text{v-v}}$, we need to estimate the probability of a collision hard enough to supply the v-v energy difference ΔE , assuming a Boltzmann velocity distribution $\sigma_{\text{v-v}} = \sigma_{\text{GKC}} \exp(-\Delta E/k_B T_e)$, where $\sigma_{\text{GKC}} = 15 \text{ \AA}^2$ is the gas kinetic cross section. For N_2O , the zero-point energy of the vibrational level just below ν_3 is approximately 350 cm^{-1} lower, giving $\sigma_{\text{v-v}} \approx 0.2\sigma_{\text{GKC}}$. But for molecules such as CH_3F , ν_0 is the only vibrational level below ν_3 , so $\sigma_{\text{v-v}}$ is negligibly small (approximately $0.005\sigma_{\text{GKC}}$ for that 1050 cm^{-1} energy separation).

Using Eqs. (2) and (3), the thermal-pool population may be estimated as

$$\begin{aligned} N_p &= \frac{k_{\text{DD}}}{2k_{\text{pool}}}(N_2 + N_3) \\ &= \frac{(3k_{\text{DD}}/2 + k_w)}{(k_{\text{DD}}/2 + k_w)} \frac{k_{\text{DD}}}{2k_{\text{pool}}} \Delta N \\ &= \tilde{k} \Delta N. \end{aligned} \quad (7)$$

The thermal population added to levels 2 and 3 acts to quench the population inversion by $(f_3 - f_2)N_p = (f_3 - f_2)\tilde{k}\Delta N$, where f_2 and f_3 are the respective thermal population fractions. Because $k_{\text{v-v}} \gg k_w$ for all but the smallest-diameter cavities and lowest pressures in N_2O , $\tilde{k} \lesssim 20$, and since $f_3 - f_2 < 10^{-3}$ for $J_L > 10$, the thermal quenching effect on ΔN is negligible. Therefore, N_p may be excluded from the three-level model for N_2O .

However, in molecules such as CH_3F and NH_3 without lower-lying vibrational levels, the thermal-pool population becomes important when vibrational relaxation mechanisms are slow and population accumulates in the pumped vibrational level, producing vibrational bottlenecking. In such cases, $k_{\text{v-v}} \rightarrow 0$, and $\tilde{k} \rightarrow 3k_{\text{DD}}/2k_{\text{pool}} = 3k_{\text{DD}}/2k_w$, which increases quadratically with pressure considering $k_{\text{DD}} \propto p$ and $k_w \propto 1/p$. Fortunately, as thermal population accumulates in the excited thermal pool, the vibrational bottleneck effect is somewhat circumvented at high pressures through additional v-v collisions involving higher-lying vibrational levels, an effect that can be simulated

by introducing an effective vibrational temperature representing the population of an ensemble of many high-lying vibrational levels [15,19].

Using the calculation of the pump absorption, pump saturation, and population inversion, one may obtain the gain coefficient γ , pump threshold P_{th} , conversion efficiency η , and output power P_{THz} of the QPML. The unsaturated gain coefficient [22] is

$$\gamma_0 = \sigma \Delta N,$$

where $\sigma = \lambda_{\text{THz}}^2 / 8\pi^2 \Delta \nu t_{\text{sp}}$ is the cross section for the lasing transition, the spontaneous emission lifetime is $t_{\text{sp}} = 3h\epsilon_0 \lambda_{\text{THz}}^3 / 16\pi^3 \mu_{23}^2$, where $\mu_{23}^2 = |\langle 2|\mu|3 \rangle|^2$ is the dipole matrix element for the laser transition, and $\Delta \nu$ is the half width of the gain profile, approximated as $\Delta \nu \approx \sqrt{\Delta \nu_D^2 + \Delta \nu_p^2}$, where $\Delta \nu_D$ and $\Delta \nu_p$ are the Doppler-broadening (for the terahertz transition) and pressure-broadening line widths, respectively.

The laser threshold occurs when the gain coefficient balances the total cavity loss α_{cell} at the terahertz laser frequency,

$$\gamma_0 = \alpha_{\text{cell}}. \quad (8)$$

The total cavity loss consists of the terahertz transmission loss through the front mirror and internal Ohmic losses. The latter can be computed analytically for the modes of a hollow metal waveguide [23], and we assume throughout this paper that the cylindrical QPML lases in the lowest-loss TE_{01} mode. From this, the threshold power can be obtained as

$$P_{\text{th}} = \frac{h\nu_{\text{IR}}}{\sigma} \frac{\alpha_{\text{cell}}}{\beta} (\pi R_{\text{cell}}^2 L) (1.5k_{\text{DD}} + k_w). \quad (9)$$

Figure 3 compares the pressure-dependent pump threshold with that calculated using the comprehensive numerical simulation [19] and the prior three-level model [12] for a cylindrical copper cavity with $R_{\text{cell}} = 0.25$ cm, $L = 15$ cm, and $T = 0.016$ for the TE_{01} mode. In the calculations, the QCL with full line width 2 MHz excites the R -branch IR transition ($J_L = 14, \nu_0 \rightarrow J = 15, \nu_3$). At low pressures dominated by pressure-independent ballistic wall collisions, $\beta \propto \alpha_{\text{IR}} L \propto p$ and $k_w \gg k_{\text{DD}}$, so $P_{\text{th}} \propto 1/p$. At higher pressures characterized by diffusive wall collisions ($k_w \propto 1/p$) and $\beta \rightarrow 1$, $P_{\text{th}} \propto k_{\text{DD}} \propto p$. These behaviors are clearly observed in Fig. 3, which shows how closely our improved three-level model agrees with the comprehensive model across all pressures, while the simpler three-level model proposed in Refs. [12,24] only works well in the low-pressure limit for which it was designed.

The output power P_{THz} is computed with the condition that the saturated gain coefficient equals the cavity loss,

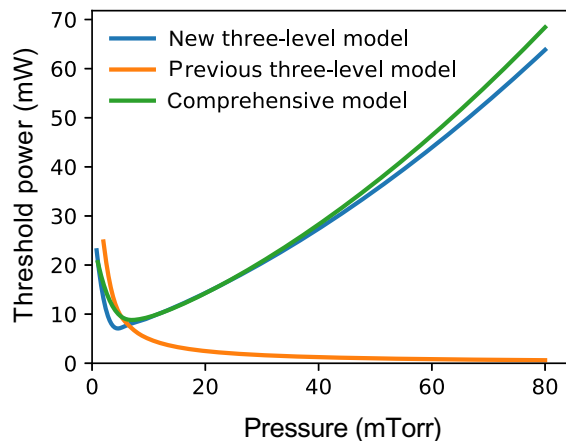


FIG. 3. The pump threshold P_{th} as a function of pressure, compared with the prior three-level model [12,24] and the comprehensive model [19], for a cylindrical copper cavity with $R_{\text{cell}} = 0.25$ cm, $L = 15$ cm, and $T = 0.016$ filled with N_2O pumped by a QCL with $\Delta \nu_{\text{QCL}} = 1$ MHz coincident with the R -branch IR transition $J_L = 14, \nu_0 \rightarrow J = 15, \nu_3$.

i.e.,

$$\gamma = \frac{\gamma_0}{1 + \Phi/\Phi_s} = \alpha_{\text{cell}}, \quad (10)$$

in which Φ is the terahertz photon flux density, $\Phi_s = k_s/\sigma$ is the saturated photon flux density, and k_s is the saturated characteristic rate. In our three-level model, $k_s = (3k_{\text{DD}}/2 + k_w)/2$ following the derivation in Ref. [22]. From this, the output power can be calculated as [22]

$$\begin{aligned} P_{\text{THz}} &= \frac{T}{2} h\nu_{\text{THz}} (\pi R_{\text{cell}}^2) \Phi \\ &= \frac{T}{2} h\nu_{\text{THz}} (\pi R_{\text{cell}}^2) \left(\frac{\gamma_0}{\alpha_{\text{cell}}} - 1 \right) \frac{k_s}{\sigma}. \end{aligned} \quad (11)$$

Figure 4 plots P_{THz} as a function of pressure with 250 mW of QCL power pumping the same transition considered in Fig. 3. The prediction of the three-level model quantitatively matches the comprehensive model to within 15%, validating the methodology outlined above. [The three-level model slightly underestimates this optimal pressure, because it slightly overestimates the IR absorption at low pressures and underestimates the threshold power (Fig. 3) at higher pressures.]

IV. CAVITY DESIGN

Thus, with the validated three-level model proposed in this paper, along with the comprehensive model [19], let us now explore how P_{THz} depends on molecular and cavity parameters in order to explore optimal cavity designs and pumping strategies. Throughout, we assume that the most powerful QCL available is being used and that the simplest

way to increase the QPML power is to increase the QCL power. Consequently, we begin the discussion by assuming a fixed QCL power of 250 mW and explore how to optimize all other design and operational parameters. Once the optimal cavity design is identified, we conclude by exploring how the QPML power increases with increasing QCL pump power.

A. Pressure

Pressure is perhaps the easiest and second most important operational parameter that a user may adjust. The pressure dependence of P_{THz} is determined by the competing pressure dependencies of γ_0 and k_s . Both of these increase at low pressure, but at higher pressures ΔN and γ_0 shrink faster than k_s grows, so an intermediate pressure produces maximal power. But underlying these behaviors is a helpful rule of thumb: the optimal pressure p^{opt} occurs as β reaches 1, because at lower pressures the pump beam is not fully absorbed while at higher pressures the gas is not fully pumped. This is illustrated in Fig. 4, which compares the IR fractional absorption β with the output power. Certainly, these effects are exacerbated at low pressure by pump saturation and at high pressure by thermal quenching, but the primary factor determining the maximum QPML power for a given transition and cavity geometry

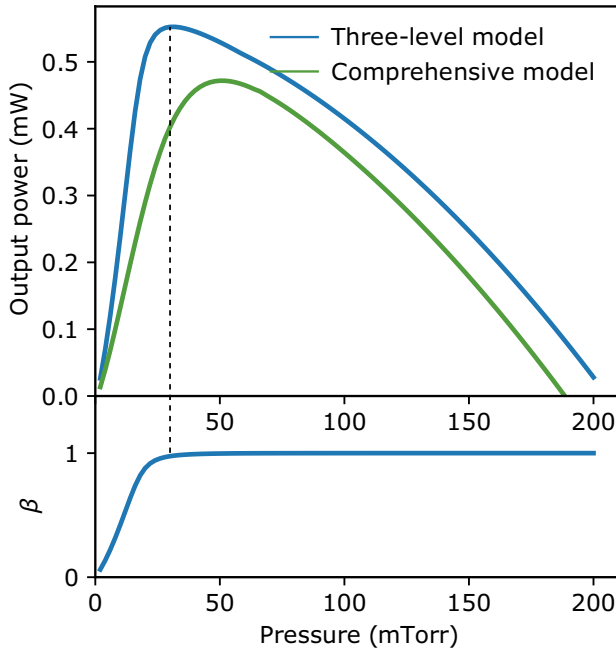


FIG. 4. The pressure-dependent QPML output power predicted by the three-level model and the comprehensive model. A 250-mW QCL pumps the R -branch transition $J = 14$, $v_0 \rightarrow J = 15$, v_3 in a cavity of radius $R_{\text{cell}} = 0.25$ cm, length $L = 15$ cm, and front-mirror transmission $T = 0.016$. The IR absorption β from the three-level model is plotted below to show that the optimal pressure occurs as β reaches 1.

is the pressure at which absorption of the QCL pump is optimized. Consequently, the calculation of β is critically important for estimating the performance of QPMLs.

B. Frequency

The frequency of the QPML also affects the maximum power achievable. Of course, the QPML is a line-tunable laser and the possible laser frequencies are the known rotational absorption transition frequencies of the molecular gain medium. The dependence of the QPML power on this frequency may be seen if Eq. (9) is used to rewrite Eq. (11) as

$$P_{\text{THz}} = \frac{\beta}{2} \left(\frac{h\nu_{\text{THz}}}{h\nu_{\text{IR}}} \right) \left(\frac{T/2L}{\alpha_{\text{cell}}} \right) (P_{\text{QCL}} - P_{\text{th}}), \quad (12)$$

with the power efficiency given by

$$\eta = \frac{\beta}{2} \left(\frac{h\nu_{\text{THz}}}{h\nu_{\text{IR}}} \right) \left(\frac{T/2L}{\alpha_{\text{cell}}} \right). \quad (13)$$

The upper limit of the power efficiency η is simply

$$\eta \leq \frac{1}{2} \left(\frac{\nu_{\text{THz}}}{\nu_{\text{IR}}} \right), \quad (14)$$

where the factor of 1/2 (preceding the Manley-Rowe limit $\eta \leq \nu_{\text{THz}}/\nu_{\text{IR}}$) comes from the fact that k_w is the same for levels 2 and 3. In the comprehensive model [19], with its larger number of energy levels and more comprehensive modeling of collisional transitions, this upper limit is somewhat relaxed, as shown in Fig. 5(a).

More importantly, since the pump frequency ν_{IR} changes little over the tuning range of the molecular gain medium, the power efficiency and output power of a QPML increase with increasing ν_{THz} , as can be seen in Fig. 5(a). This Manley-Rowe-related trend indicates that, for $P_{\text{QCL}} \gg P_{\text{th}}$ and all other factors being equal, higher power can be obtained at higher QPML frequencies as the energy efficiency of converting IR photons to terahertz photons increases. This is a tremendously important effect, because otherwise the terahertz frequency dependence of P_{THz} would mirror the IR frequency dependence of α_{IR} for a fixed-length cavity. Specifically, for N_2O , the R -branch transition with the largest α_{IR} occurs at $J_L^{\text{max}} = 15$, naively suggesting that the maximum P_{THz} occurs at only $\nu_{\text{THz}}^{\text{max}} \approx 0.399$ THz. Instead, the Manley-Rowe effect pushes the transition that produces the most laser power much higher, toward $J_L \rightarrow 40$ and $\nu_{\text{THz}}^{\text{max}} \rightarrow 1$ THz.

Since the population of J_L decreases as ν_{THz} increases above J_L^{max} , the optimal pressure p^{opt} to achieve maximum laser power must increase with increasing J_L [Fig. 5(b)]. However, increasing the pressure also increases P_{th} (Fig. 3), so Eq. (12) reveals how the laser power drops precipitously below the Manley-Rowe limit as P_{th}

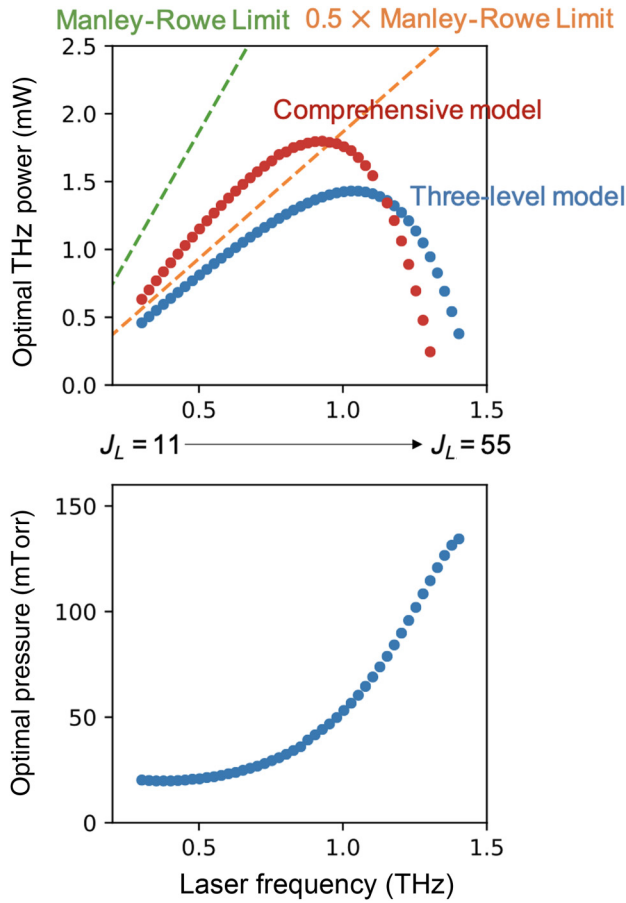


FIG. 5. (a) The laser frequency-dependent maximum output power for $J_L = 11$ to 51. (b) The optimal molecular pressure for (a) predicted by the three-level model for each laser frequency.

approaches P_{QCL} with increasing J_L , thus establishing the high-frequency limit for laser operation.

C. Cavity loss

The cavity loss, which deleteriously increases P_{th} [Eq. (9)] and decreases P_{THz} [Eq. (12)], is the next most important factor determining the QPML power. The cavity loss is determined by two terms in $\alpha_{\text{cell}} = \alpha_T + \alpha_o$, where α_o is the Ohmic loss of the metallic cavity and

$$\alpha_T = -\frac{\ln(1-T)}{2L} \approx \frac{T}{2L}. \quad (15)$$

is the transmission loss from the front mirror. For $T = 0.016$ and $L = 15$ cm, $\alpha_T \approx 0.053$ m⁻¹.

The Ohmic loss for the lowest-loss TE₀₁ mode in the cylindrical cavity is [23]

$$\alpha_o = \frac{R_s}{R_{\text{cell}} \eta_0 \sqrt{1 - (x_0/k_0 R_{\text{cell}})^2}} \left(\frac{x_0}{k_0 R_{\text{cell}}} \right)^2, \quad (16)$$

where $\eta_0 = 377$ Ω is the free-space impedance, $k_0 = 2\pi \nu_{\text{THz}}/c$ is the wave number, $x_0 = 3.83$ is the Bessel-function zero for the TE₀₁ mode, and $R_s = \sqrt{\pi \nu_{\text{THz}} \mu_0 / \sigma_{\text{Cu}}}$ is the rf sheet resistance (for which the conductivity of the copper cavity is σ_{Cu}). For frequencies far above the waveguide cutoff, we can neglect the $\sqrt{1 - (x_0/k_0 R_{\text{cell}})^2}$ term and the Ohmic loss becomes

$$\alpha_o = \left(\frac{x_0}{k_0} \right)^2 \frac{R_s}{\eta_0 R_{\text{cell}}^3}. \quad (17)$$

Note that the Ohmic loss decreases with the cell radius as $1/R_{\text{cell}}^3$ and with the laser frequency as $\nu_{\text{THz}}^{-3/2}$, the latter contributing to the improved high-frequency performance of the laser. (However, cavity alignment becomes more challenging at high frequency, an effect not considered here, as our calculation assumes a perfectly aligned cavity.) For the N₂O QPML, we have $\alpha_o \approx 0.00634/(J_L + 1)^{3/2} R_{\text{cell}}^3$ m⁻¹ with R_{cell} in cm.

The cavity loss α_{cell} is usually dominated by the transmission loss [Eq. (15)], which is much larger than the Ohmic loss [Eq. (16)] for typical compact cavities ($R_{\text{cell}} > 0.1$ cm, $L < 1$ m, $T > 0.01$). At first glance, Eq. (9) appears to imply a linear relation of threshold power P_{th} on α_{cell} . However, the relation is actually nonlinear, because the cavity loss also affects β . Figure 6 shows how P_{th} increases with α_{cell} . The curves are linear at higher pressures as $\beta \rightarrow 1$ but become superlinear when pressure, α_{IR} , or β are low. This again shows the importance of β and its accurate self-consistent modeling for the cavity design.

In the pressure regime for which $\beta \rightarrow 1$, which occurs at or above p^{opt} , the output power [Eq. (12)] from such a compact cavity may be approximated as

$$P_{\text{THz}} \approx \frac{1}{2} \frac{\nu_{\text{THz}}}{\nu_{\text{IR}}} P_{\text{QCL}}, \quad (18)$$

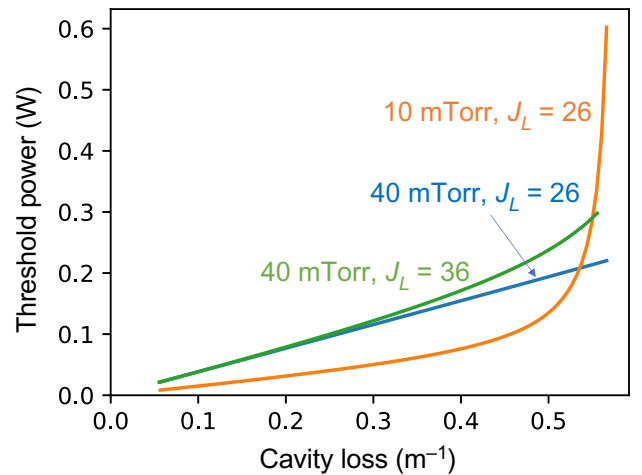


FIG. 6. P_{th} as a function of the total cavity loss for two transitions and two pressures.

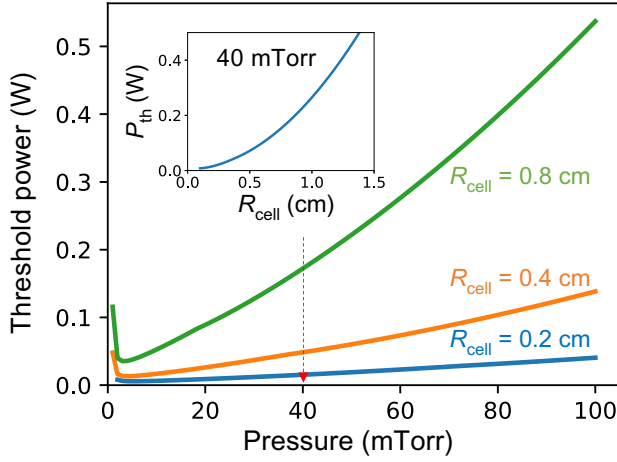


FIG. 7. P_{th} plotted for QCL pump excitation of $J_L = 26$ as a function of pressure for cavity radii $R_{\text{cell}} = 0.2, 0.4,$ and 0.8 cm with a fixed cavity length $L = 15$ cm and front-mirror transmission $T = 0.016$. The inset shows how P_{th} increases quadratically with R_{cell} .

when the pump power is much larger than the threshold power. The way in which P_{th} and P_{THz} depend on the cavity parameters $R_{\text{cell}}, L,$ and T is addressed next.

D. Cavity radius

The cavity radius primarily affects the threshold power. Equation (9) shows that for the compact cavities considered here, with fixed T and $\alpha_o \ll \alpha_T$, P_{th} increases quadratically with the cavity radius. Figure 7 plots the threshold as a function of pressure for three different cavity radii. As described above, P_{th} increases quasilinearly with pressure except at very low pressures, but note how much P_{th} increases as the cavity radius increases for a given pressure. This occurs because of the assumption that the QCL pump uniformly illuminates the cavity, so the pump rate must decrease with the cavity cross section as $1/R_{\text{cell}}^2$. The inset plots P_{th} as a function of R_{cell} with fixed pressure (40 mTorr), to confirm the quadratic relationship between the lasing threshold and the cavity radius. Of course, a larger radius becomes detrimental in other ways, such as when the cavity becomes multimoded or the pump beam does not spread enough to fill the whole diameter.

Figure 8(a) plots the corresponding QPML output powers P_{THz} as a function of pressure for the same three cavities using a 250-mW QCL pump. Both the peak pressure p^{opt} and the maximum “cutoff” pressure at which $P_{\text{THz}} = 0$ increase with decreasing cavity radius, a direct consequence of the quadratic dependence of P_{th} on R_{cell} . As indicated above, the pressure p^{opt} at which peak power is achieved occurs as $\beta \rightarrow 1$. Figure 8(b) illustrates this by plotting β over the same pressure range for all three radii. Note how β increases faster with pressure for larger radii, a consequence of Eq. (12), which shows that P_{THz} is

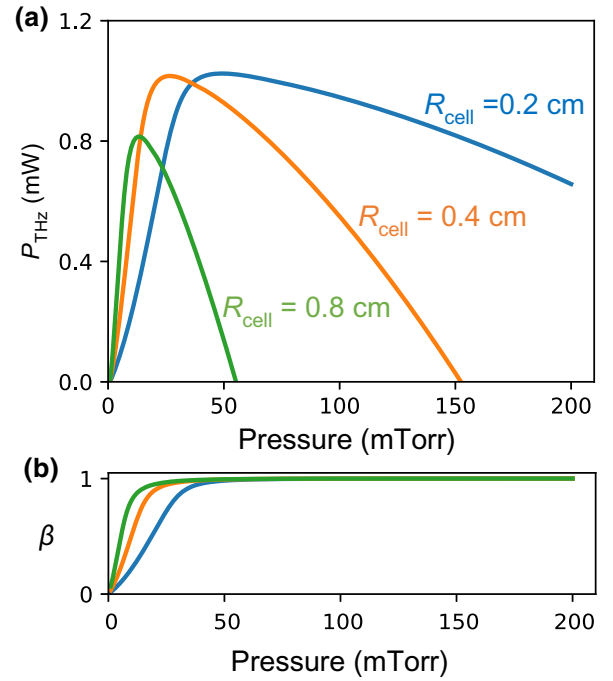


FIG. 8. The pressure-dependent terahertz output power (a) and IR absorption β (b) for cavity radii $R_{\text{cell}} = 0.2, 0.4,$ and 0.8 cm with a fixed cavity length $L = 15$ cm, front-mirror transmission $T = 0.016$, and 250-mW excitation of the $J_L = 26$ transition.

proportional to β . Since the slope is larger in Fig. 8(a) at low pressures for cavities with larger R_{cell} , cavities with smaller radii can operate over a much wider (and more forgiving) range of pressures than those with larger radii.

E. Cavity length

The cavity length affects the optimal operation pressure but does not greatly affect the threshold power in the regime considered here, $\alpha_o \ll \alpha_T \approx \alpha_{\text{cell}}$, for which the limiting case of Eq. (9) becomes

$$P_{\text{th}} \approx (h\nu_{\text{IR}})(\pi R_{\text{cell}}^2 T)(1.5k_{\text{DD}} + k_w)/2\sigma\beta. \quad (19)$$

The solid lines in Fig. 9 confirm this perhaps surprising result that P_{th} weakly depends on L . The reason is simple: the β term captures the effects of multiple round trips and pump saturation, so the pump beam passes through the cavity as many times as necessary for all pump photons to be absorbed. Indeed, the very slight dependence on cavity length comes from the additional losses of the IR pump in a short cavity, as multiple round trips allow a small portion to be absorbed by the front and back metallic mirrors and leak through the output coupler (T_{IR}) each round trip. As noted above, this leakage ultimately limits the number of round trips possible in a given cavity and this limit explains why $\beta < 1$ at low pressures: too many pump photons are lost before being absorbed by the molecular gain medium.

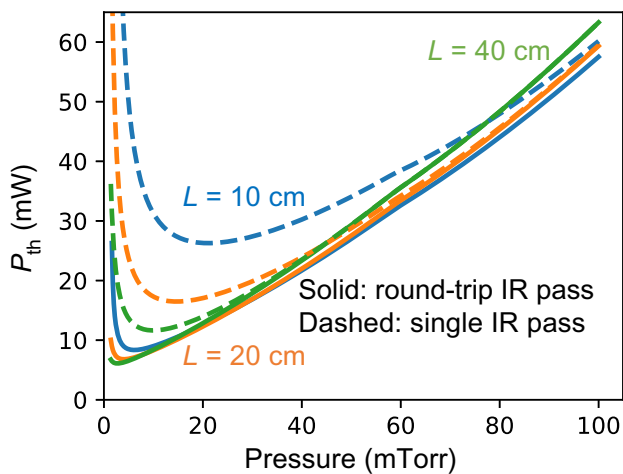


FIG. 9. Solid lines: Pressure-dependent P_{th} for cavity lengths $L = 10, 20,$ and 40 cm with a fixed cavity radius $R_{\text{cell}} = 0.25$ cm, front-mirror transmission $T = 0.016$, and pump excitation of the $J_L = 26$ transition. Dashed lines: the same calculations but assuming only a single IR pass through the cavity without back reflection.

If the model only assumes a single pass for the IR pump, as shown in the dashed lines of Fig. 9, P_{th} becomes larger and more sensitive to L until the molecular pressure is high enough to absorb all the pump photons.

The fact that this metallic cavity geometry allows multiple round trips of the IR pump provides a significant advantage in reducing laser size. Most prior work on low-pressure OPFIR lasers has used very long cavities to maximize absorption of pump photons in a single pass. Regardless of geometry, note that the peak power occurs as $\beta \rightarrow 1$, because this is the first pressure at which all the pump photons are absorbed by the molecular gain medium. As the pressure increases above p^{opt} , pump photons are fully absorbed in the front portion of the cavity, leaving many molecules unpumped, an indication that the cavity is too long. Operation at higher pressures has been a principal motivation for the compact-cavity concept [15,19].

Figure 10(a) plots the output power as a function of pressure for cavity lengths of $L = 10, 20,$ and 40 cm and a fixed radius $R_{\text{cell}} = 0.25$ cm. These three curves are more similar than they are different, with comparable peak output powers occurring at the pressure where $\beta \rightarrow 1$, as can be seen in Fig. 10(b). In short cavities, the effects of pump saturation cause more round trips before complete absorption, so more of the IR pump is lost through leakage. Consequently, shorter cavities require more pressure than longer cavities to reach their peak absorption and peak power. However, the high-pressure behaviors and cutoffs are similar for all three cavity lengths, a consequence of how insensitive P_{th} is to L (in contrast with its strong sensitivity to R_{cell} seen in Fig. 8).

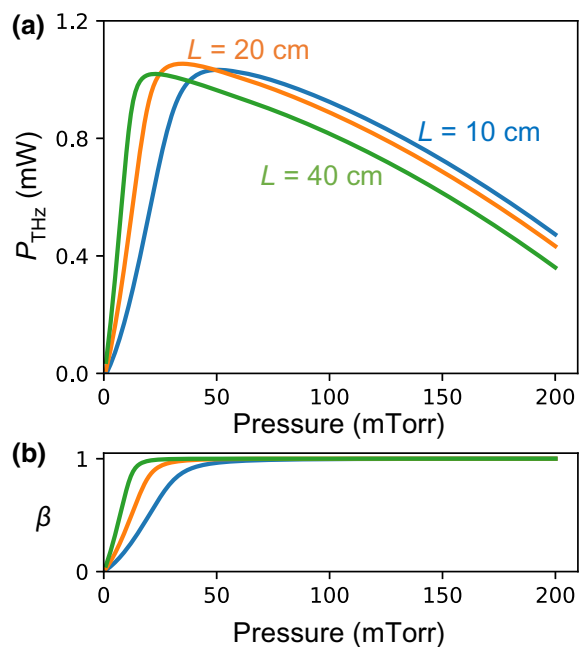


FIG. 10. The terahertz output power and IR fractional absorption β for cavity lengths $L = 10, 20,$ and 40 cm with a fixed cavity radius $R_{\text{cell}} = 0.25$ cm, front-mirror transmission $T = 0.016$, and 250-mW excitation of the $J_L = 26$ transition.

F. Output Coupler Transmission

The output-coupler transmission T at the emission frequency ν_{THz} should be adjusted to maximize the output power P_{THz} . Note that T_{THz} is not the same as T_{IR} , and how they differ depends on the type of output coupler used. If it is a partially reflecting mirror, then the spectral dependence of the reflectivity and absorptivity of the window determines T_{THz} and T_{IR} . If it is a circular pinhole in an otherwise highly reflective circular mirror, then T_{IR} is likely the ratio of the geometrical areas of the pinhole and mirror, while T_{THz} is approximated by the spatial overlap of the lasing mode with the pinhole. (The radiation through a very subwavelength hole would require an entirely different approach [25].) Because the pinhole must be large enough for radiation to be emitted through ($\nu_{\text{cutoff}} = 1.84c/2\pi R_{\text{pinhole}} \approx 88/R_{\text{pinhole}}$ GHz for R_{pinhole} in millimeters), the requirement that $\nu_{\text{cutoff}} < \nu_{\text{THz}}$ determines the minimum possible value of T for a given laser transition. To maintain a constant T with increasing cavity radius, the pinhole diameter must also increase. Even larger pinhole diameters may be desired to reduce diffraction of the emitted terahertz beam, at the cost of larger values of T and cavity loss, and lower values of β due to more IR leakage.

Given an understanding of these constraints, the optimal transmissivity may be obtained from $dP_{\text{THz}}/dT = 0$,

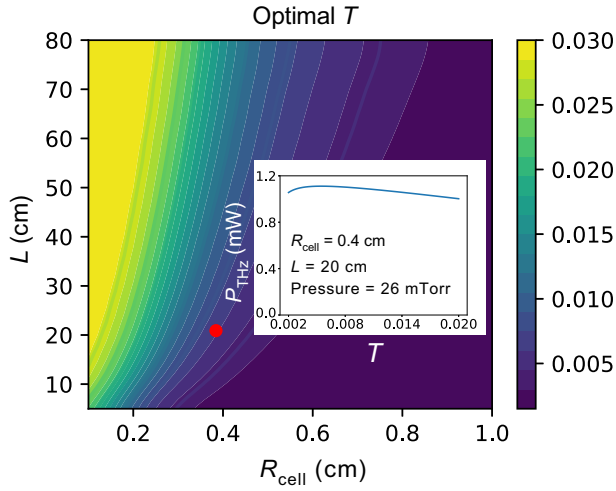


FIG. 11. The optimal front-mirror transmission coefficient T as a function of the cavity radius R_{cell} and length L , each operating at p^{opt} for the $J_L = 26$ transition pumped by a 250-mW QCL. The inset shows how the output power is relatively insensitive to T for a cell with $R_{\text{cell}} = 0.4$ cm, $L = 20$ cm, and pressure = 26 mTorr (red dot).

so using Eqs. (12) and (9), we can derive

$$T_{\text{opt}} = \sqrt{\frac{4\beta\sigma\alpha_oLP_{\text{QCL}}}{h\nu_{\text{IR}}(\pi R_{\text{cell}}^2)(1.5k_{\text{DD}} + k_w)}} - 2\alpha_oL. \quad (20)$$

This complex equation contains most of the parameters already considered, suggesting that T_{opt} should be decided last, after optimal values for all these other parameters have been ascertained. As can be seen in Eq. (12), P_{THz} is rather insensitive to T in the common regime for which $\alpha_{\text{cell}} \approx \alpha_T$, fortuitously allowing us to pick a fixed front-mirror transmissivity without sacrificing much laser efficiency. To illustrate this insensitivity, consider a cavity with $R_{\text{cell}} = 0.4$ cm, $L = 20$ cm, pumped with a 250-mW QCL on the $J_L = 26$ transition, and filled with 26-mTorr of N_2O , for which the optimal front-mirror transmission coefficient is found to be $T_{\text{opt}} = 0.0056$. Figure 11 explores how T_{opt} depends on R_{cell} and L for this same transition for a range of cavity geometries, each operating at the optimal lasing pressure p^{opt} . Note that very highly reflective output couplers are required, with $T < 1\%$ for all but the smallest-diameter cavities. Interestingly, T_{opt} is rather insensitive to L and decreases slowly with increasing R_{cell} . As the inset illustrates, the output power varies little as T varies from 0.002 to 0.020, so a constant value such as $T = 0.01$ may be set with little sacrifice in performance.

G. Optimal cavity design

Optimal cavity design encompasses all these parameters to create conditions for maximum QPML power for a given QCL pump power. The objective is to convert

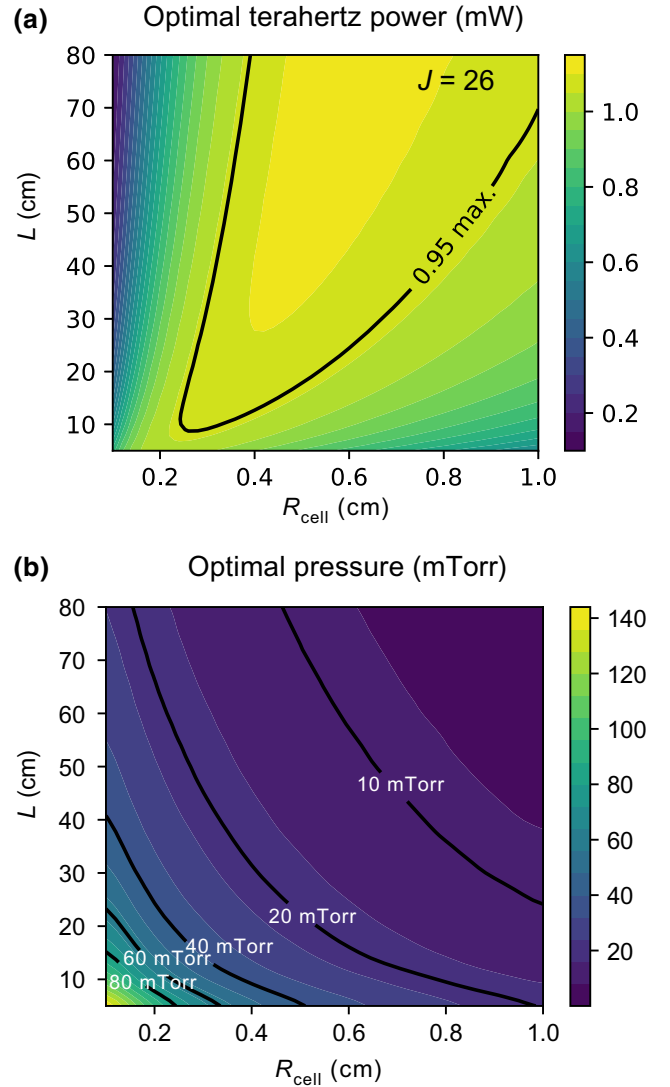


FIG. 12. (a) The maximum terahertz power as a function of the cavity radius and length for the $J_L = 26$ transition with 250-mW QCL pump power. Each value of P_{THz} is obtained at p^{opt} with fixed $T = 0.01$. (b) The corresponding optimal pressure p^{opt} for each cavity geometry in (a).

infrared photons to terahertz photons efficiently, thereby approaching the Manley-Rowe limit as closely as possible. To illustrate how to ascertain the optimal cavity geometry using this model, Fig. 12(a) plots the maximum output power as a function of the cavity radius and length for the $J_L = 26$ transition pumped by a 250-mW QCL with $T = 0.01$. Half the Manley-Rowe limit [Eq. (18)] for this transition at $\nu_{\text{THz}} = 0.672$ THz and $\nu_{\text{IR}} = 67.3$ THz (2243.761 cm^{-1}) is $P_{\text{THz}} = 1.25$ mW.

As can be seen in Fig. 12(a), a wide range of cavity geometries approach this maximum power limit, indicating that QPMLs are rather tolerant of nonideal cavity dimensions as long as they are operated at p^{opt} . Since this optimal

pressure for maximum laser power depends on the cavity radius R_{cell} and length L , the powers P_{THz} plotted in Fig. 12(a) are calculated for the corresponding p^{opt} plotted in Fig. 12(b). As expected from the above discussion, p^{opt} decreases with increasing R_{cell} and L . However, P_{THz} has a more complex dependence on the radius and length, with maximum power achieved for an accommodating range of cavity radii ($0.4 < R_{\text{cell}} < 0.8$ cm) and lengths ($L > 30$ cm) when operated at p^{opt} .

In general, excellent performance may be obtained from compact-cavity geometries ($R_{\text{cell}} < 1$ cm, $L < 1$ m) operating at low pressures ($p^{\text{opt}} < 100$ mTorr) with low front-mirror transmission ($T \sim 0.01$). Although the maximum power for this transition and pump power occurs in a cavity with $R_{\text{cell}} = 0.8$ cm, and $L = 178$ cm, the 95% contour line shows how forgiving the QPML is to nonideal cavity geometries. This is of particular importance for practical applications where low-volume geometries are favored. In this example, a compact laser cavity with $R_{\text{cell}} = 0.4$ cm and $L = 20$ cm can achieve more than 95% of the maximum output power but with approximately $40\times$ smaller volume than the $R_{\text{cell}} = 0.8$ cm, $L = 178$ cm “optimal” cavity.

Finally, let us consider how these parameters depend on the frequency of the QPML. Figures 13(a)–13(c) plot the maximum terahertz power that can be achieved for the $J_L = 16, 26,$ and 36 transitions, with corresponding frequencies $\nu_{\text{THz}} = 423, 672,$ and 921 GHz. The maximum output power increases with J_L as expected by the Manley-Rowe effect [26]. Since $P_{\text{QCL}} = 250$ mW $\gg P_{\text{th}}$, the maximum possible powers may be estimated from Eq. (18) to be 0.79, 1.25, and 1.71 mW, respectively. Again, the black contour lines denote the broad range of cavity geometries that achieve 95% of the maximum output power. It can be seen that a single cavity geometry may be selected to achieve near-optimal performance for all three transitions and every transition between. Stated another way, the cavity geometry does not need to change from transition to transition to achieve near-optimal performance, as long as the laser operates at p^{opt} for that transition.

As compared to the optimal configuration for all transitions, one such compact geometry ($R_{\text{cell}} = 0.4$ cm, $L = 20$ cm, $T = 0.01$), represented by the blue dot in Figs. 13(a)–13(c), only loses 5% laser performance with a volume 10 – $100\times$ smaller. The fact that a single compact cigar-sized cavity can perform nearly optimally across the range of operational frequencies bodes well for the technological viability of the QPML concept.

V. PUMP-POWER DEPENDENCE

Now that the optimal cavity geometry is understood, we may revisit the one parameter held constant throughout this analysis: the QCL pump power. Using the near-optimal

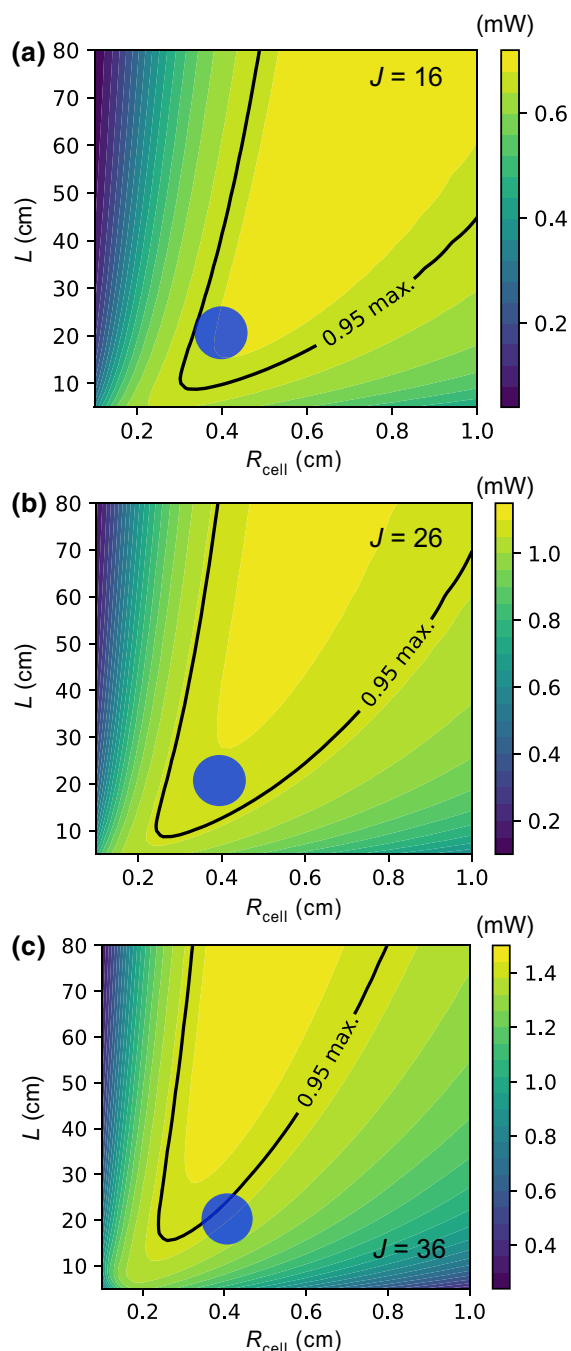


FIG. 13. The maximum terahertz power for (a) $J_L = 16$, (b) $J_L = 26$, and (c) $J_L = 36$ pumped by a 250-mW QCL. Each point is obtained by optimizing the molecular pressure to maximize P_{THz} with a fixed front-mirror transmission $T = 0.01$. The blue dot indicates a compact-cavity geometry ($R_{\text{cell}} = 0.4$ cm, $L = 20$ cm) that achieves at least 95% of the maximum possible output power for all transitions.

compact-cavity configuration $R_{\text{cell}} = 0.4$ cm, $L = 20$ cm, $T = 0.01$, Fig. 14(a) plots the maximum terahertz power (solid lines) and half the Manley-Rowe limit (dashed lines) as a function of QCL pump power for different transitions

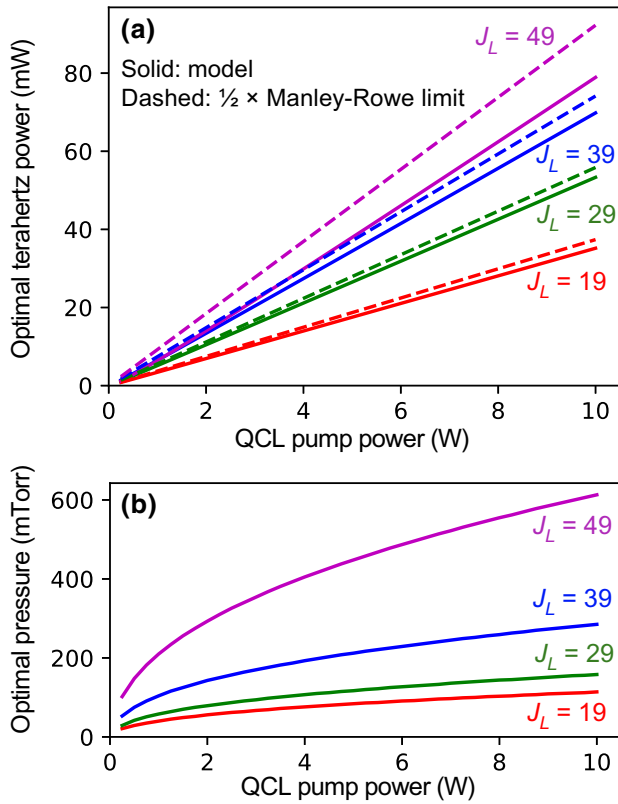


FIG. 14. (a) The optimal terahertz power with varying QCL pump power for different transitions and (b) the corresponding optimal molecular pressures, using the near optimal cavity configuration ($R_{\text{cell}} = 0.4$ cm, $L = 20$ cm, $T = 0.01$) obtained previously.

$J_L = 19, 29, 39,$ and 49 , corresponding to frequencies near 0.498, 0.747, 0.996, and 1.245 THz, respectively. Because of the Manley-Rowe effect, the general trend is that optimal terahertz power increases with increasing J_L and corresponding emission frequency. However, as J_L and frequency increase, pump saturation and low infrared absorption increasingly cause the output power to deviate from the theoretical optimal (dashed lines), ultimately leading to the precipitous drop in power at the highest frequencies seen in Fig. 5.

Although the same cavity may be used for all these transitions, achieving optimal terahertz power as the QCL pump power increases requires overcoming pump saturation by increasing the molecular pressure, as shown in Fig. 14(b). For the same reason, the optimal pressure also increases with the transition number J_L to achieve sufficiently large α_{IR} as the fractional population of J_L drops.

With a fixed 10-W QCL pump, Fig. 15 plots the optimal terahertz power for transitions $J_L = 15$ ($\nu_{\text{THz}} = 400$ GHz) to $J_L = 63$ ($\nu_{\text{THz}} = 1.6$ THz), similar to Fig. 5 but with a much higher pump power. With a 10-W QCL, the maximal terahertz power achievable is 79 mW for $J_L = 49$ near

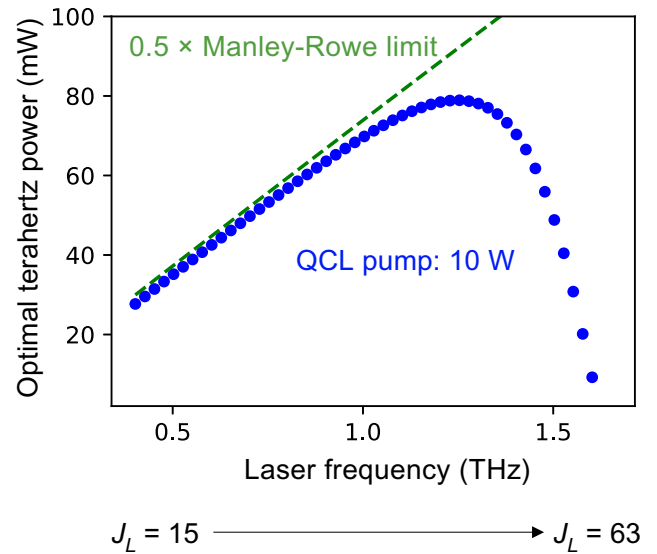


FIG. 15. The optimal terahertz power for all transitions $J_L = 15$ ($\nu_{\text{THz}} = 400$ GHz) to $J_L = 63$ ($\nu_{\text{THz}} = 1.6$ THz) with a fixed 10-W QCL pump power.

1.245 THz, far higher in frequency than the peak of the R -branch infrared absorption spectrum at $J_L = 15$. Indeed, by comparing Figs. 5 and 15, we see that as the pump power increases, the increasing optimal pressure and the Manley-Rowe effect combine to increase the frequency at which the peak terahertz power may be produced from a QPML. Multiwatt-class QCLs are becoming commercially available, opening up the exciting prospect that N_2O , NH_3 , and other QPML-gain media will soon be able to produce tens, even hundreds, of milliwatts in the region above 1 THz, a region currently devoid of comparably powerful tunable narrow-line-width sources [27].

VI. CONCLUSION

In this work, an improved three-level model of QCL-pumped molecular lasers is derived that accurately describes the nonlinear infrared absorption, including pump saturation, recycling of the pump beam within the cavity, and the essential collision physics. This improved model, validated by the comprehensive model, allows us to study quantitatively how the laser performance is influenced by the pump strategies and cavity parameters. Our calculations find that a compact N_2O QPML cavity ($R_{\text{cell}} = 0.4$ cm and $L = 20$ cm) is able to achieve 95% of the maximum laser output power across almost all laser transitions with only 2.5% of the volume of a nominally optimized cavity.

Throughout the paper, N_2O is chosen as the gain molecule, but the model and the design principles derived from it are universal and easily applied to other candidate linear molecules such as HCN, OCS, and CO. Extension of the model to very high pressures and more complex

molecules such as CH_3F and NH_3 could also be made, requiring the inclusion of additional collisional relaxation processes, but the results derived herein may be applied to those molecules without loss of generality. As such, the improved three-level model introduced here may be used to assess and achieve the potential of powerful broadly tunable QPMLs as a solution to the terahertz-gap source problem.

ACKNOWLEDGMENTS

This work was funded in part by the U.S. Army Research Office through the Institute for Soldier Nanotechnologies under Award No. W911NF-18-2-0048. We are also grateful to F. Capasso, P. Chevalier, and A. Amirzhan for helpful conversations.

- [1] T. Nagatsuma, G. Ducournau, and C. C. Renaud, Advances in terahertz communications accelerated by photonics, *Nat. Photonics* **10**, 371 (2016).
- [2] A. Maestrini, J. S. Ward, J. J. Gill, C. Lee, B. Thomas, R. H. Lin, G. Chattopadhyay, and I. Mehdi, A frequency-multiplied source with more than 1 mW of power across the 840–900-GHz band, *IEEE Trans. Microw. Theory Tech.* **58**, 1925 (2010).
- [3] R. L. Ives, C. Kory, M. Read, J. Neilson, M. Caplan, N. Chubun, S. Schwartzkopf, and R. Witherspoon, in *Terahertz for Military and Security Applications (AeroSense, Orlando, Florida, United States, 2003)*, Vol. 5070, p. 71.
- [4] J. H. Booske, R. J. Dobbs, C. D. Joye, C. L. Kory, G. R. Neil, G.-S. Park, J. Park, and R. J. Temkin, Vacuum electronic high power terahertz sources, *IEEE Trans. Terahertz Sci. Technol.* **1**, 54 (2011).
- [5] R. Köhler, A. Tredicucci, F. Beltram, H. E. Beere, E. H. Linfield, A. G. Davies, D. A. Ritchie, R. C. Iotti, and F. Rossi, Terahertz semiconductor-heterostructure laser, *Nature* **417**, 156 (2002).
- [6] K. McIntosh, E. Brown, K. Nichols, O. McMahon, W. DiNatale, and T. Lyszczarz, Terahertz photomixing with diode lasers in low-temperature-grown GaAs, *Appl. Phys. Lett.* **67**, 3844 (1995).
- [7] K. Evenson, D. Jennings, and F. Petersen, Tunable far-infrared spectroscopy, *Appl. Phys. Lett.* **44**, 576 (1984).
- [8] M. Inguscio, P. D. Natale, and L. Veseth, Isotopic shift in atomic fine structure: Theory and experiment for oxygen transitions in the far infrared, *Comments At., Mol. Phys.* **30**, 3 (1994).
- [9] A. Pagies, G. Ducournau, and J.-F. Lampin, in *2016 41st International Conference on Infrared, Millimeter, and Terahertz waves (IRMMW-THz)* (IEEE, 2016), p. 1.
- [10] A. Pagies, G. Ducournau, and J.-F. Lampin, Low-threshold terahertz molecular laser optically pumped by a quantum cascade laser, *APL Photonics* **1**, 031302 (2016).
- [11] A. Pagies, G. Ducournau, and J.-F. Lampin, in *2017 42nd International Conference on Infrared, Millimeter, and Terahertz Waves (IRMMW-THz)* (IEEE, 2017), p. 1.
- [12] P. Chevalier, A. Armizhan, F. Wang, M. Piccardo, S. G. Johnson, F. Capasso, and H. O. Everitt, Widely tunable compact terahertz gas lasers, *Science* **366**, 856 (2019).
- [13] J.-F. Lampin, A. Pagies, G. Santarelli, J. Hesler, W. Hansel, R. Holzwarth, and S. Barbieri, Quantum cascade laser-pumped terahertz molecular lasers: Frequency noise and phase-locking using a 1560 nm frequency comb, *Opt. Express* **28**, 2091 (2020).
- [14] T. Chang, T. Bridges, and E. Burkhardt, CW submillimeter laser action in optically pumped methyl fluoride, methyl alcohol, and vinyl chloride gases, *Appl. Phys. Lett.* **17**, 249 (1970).
- [15] H. O. Everitt, D. D. Skatrud, and F. C. DeLucia, Dynamics and tunability of a small optically pumped cw far-infrared laser, *Appl. Phys. Lett.* **49**, 995 (1986).
- [16] R. McCormick, H. Everitt, F. DeLucia, and D. Skatrud, Collisional energy transfer in optically pumped far-infrared lasers, *IEEE J. Quantum Electron.* **23**, 2069 (1987).
- [17] H. O. Everitt and F. C. De Lucia, Rotational energy transfer in small polyatomic molecules, *Adv. At., Mol. Opt. Phys.* **35**, 331 (1995).
- [18] S.-L. Chua, C. A. Caccamise, D. J. Phillips, J. D. Joannopoulos, M. Soljačić, H. O. Everitt, and J. Bravo-Abad, Spatio-temporal theory of lasing action in optically-pumped rotationally excited molecular gases, *Opt. Express* **19**, 7513 (2011).
- [19] F. Wang, J. Lee, D. J. Phillips, S. G. Holliday, S.-L. Chua, J. Bravo-Abad, J. D. Joannopoulos, M. Soljačić, S. G. Johnson, and H. O. Everitt, A high-efficiency regime for gas-phase terahertz lasers, *Proc. Natl. Acad. Sci. USA* **115**, 6614 (2018).
- [20] H. O. Everitt III, Ph.D. thesis, Department of Physics, Trinity College of Arts and Sciences, Duke University (1990).
- [21] I. Gordon, *et al.*, The HITRAN2016 molecular spectroscopic database, *J. Quant. Spectrosc. Radiat. Transfer* **203**, 3 (2017), HITRAN2016 Special Issue.
- [22] B. E. A. Saleh and M. C. Teich, *Fundamentals of Photonics*, Vol. 22 (Wiley, New York, NY, 1991).
- [23] R. Bansal, *Fundamentals of Engineering Electromagnetics* (CRC Press, Boca Raton, FL, 2006).
- [24] P. Chevalier, A. Amirzhan, F. Wang, M. Piccardo, S. G. Johnson, F. Capasso, and H. O. Everitt, Response to comment on widely tunable compact terahertz gas lasers, [ArXiv:2008.11691](https://arxiv.org/abs/2008.11691) (2020).
- [25] H. A. Bethe, Theory of diffraction by small holes, *Phys. Rev.* **66**, 163 (1944).
- [26] J. Manley and H. Rowe, Some general properties of nonlinear elements—part I. General energy relations, *Proc. IRE* **44**, 904 (1956).
- [27] R. A. Lewis, A review of terahertz sources, *J. Phys. D: Appl. Phys.* **47**, 374001 (2014).

Correction: The previously published Figure 5 contained axis label errors introduced during the production cycle and has been replaced.